

Controlling strongly correlated dust clusters with lasers

Hauke Thomsen¹, Patrick Ludwig¹, Michael Bonitz¹, Jan Schablinski², Dietmar Block², André Schella³ and André Melzer³

¹ Institut für Theoretische Physik und Astrophysik,
Christian-Albrechts-Universität zu Kiel, 24098 Kiel, Germany

² Institut für Experimentelle und Angewandte Physik,
Christian-Albrechts-Universität zu Kiel, 24098 Kiel, Germany

³ Institut für Physik, Ernst-Moritz-Arndt-Universität Greifswald,
17487 Greifswald, Germany

E-mail: thomsen@theo-physik.uni-kiel.de,
ludwig@theo-physik.uni-kiel.de, bonitz@physik.uni-kiel.de,
schablinski@physik.uni-kiel.de, block@physik.uni-kiel.de,
schella@physik.uni-greifswald.de, melzer@physik.uni-greifswald.de

Abstract. The most attractive feature of dusty plasmas is the possibility to create strong correlations at room temperatures. At the same time, these plasmas allow for a precise diagnostics with single-particle resolution. From such measurements, the structural properties of finite two-dimensional (2D) clusters and three-dimensional (3D) spherical crystals in nearly harmonic traps–Yukawa balls–have been explored in great detail. Their structural properties–the shell compositions and the order within the shells–have been investigated and good agreement to theoretical predictions was found. Open questions on the agenda are the excitation behavior, the structural changes, and phase transitions that occur at elevated temperature.

In order to increase the dust temperature in the experiment various techniques have been used. Among them, laser heating appears to have unique capabilities because it affects only the dust particles, leaving the lighter plasma components unchanged. Here we report on recent experimental results where laser heating methods were further improved and applied to finite 2D and 3D clusters. Comparing to simulations, we demonstrate that this indeed allows to increase the temperature in a controlled manner. For the analysis of thermodynamics and phase transitions in these finite systems, we present theoretical and experimental results on the basis of the instantaneous normal modes, pair distribution function and the recently introduced center-two-particle distribution function.

1. Introduction

Complex plasmas differ from traditional plasmas in a number of respects: in addition to electrons, ions and neutral atoms, they can possibly contain molecules. This may lead to substantial chemical reactivity or cluster growth of macroscopically large “dust” particles, see e.g. [1–3]. Here, we focus on plasmas containing comparatively large (typically micrometer sized) particles which are commonly called “dust” particles. These spherical plastic particles of almost uniform size become highly charged when immersed into the plasma. In a radio frequency (rf) discharge, the electron temperature is way above the ion temperature resulting in a higher impact rate of electrons onto the originally neutral particles, compared to the ions. As a consequence the particles become negatively charged, with the charge reaching values on the order of $Q_d = \mathcal{O}(-10\,000\,e)$ elementary charges [4]. It is due to this high negative charge that the dust particles are strongly interacting with each other, and the dust component of the plasma becomes strongly coupled. At the same time electrons and ions are only weakly coupled. Strong correlation effects are presently of high interest in large variety of fields, including condensed matter, dense plasmas (such as warm dense matter), ultracold gases or the quark-gluon plasma. In fact, dusty plasmas serve as a prototype for studying correlation phenomena, e.g. [5].

To have a quantitative measure of correlation effects in these highly non-ideal systems, it has been common to use the Coulomb coupling parameter Γ that relates the mean Coulomb interaction energy of two particles to the thermal energy as

$$\Gamma = \frac{Q_d^2}{4\pi\epsilon_0 b_{\text{WS}}} \frac{1}{k_B T_d}, \quad (1)$$

where the Coulomb interaction is estimated by the one of two particles separated by the Wigner-Seitz radius, that is related to the density by $n^{-1} = 4\pi b_{\text{WS}}^3/3$ in 3D ($n^{-1} = \pi b_{\text{WS}}^2$ in 2D), and T_d is the kinetic temperature that corresponds to the dust particles’ random motion. In weakly non-ideal, conventional plasmas $\Gamma \ll 1$. If Γ exceeds unity, the system is strongly coupled and the particle arrangement exhibits an increasingly long range order, giving rise to liquid-like and solid-like behavior. Strictly, the definition (1) is an appropriate measure for the potential energy only when the pair interaction is Coulombic. In the case of screening, the effective coupling parameter depends on the screening length λ_D [6]. For the results reported in this paper, the dust-dust interaction is moderately screened and the definition (1) is sufficiently accurate.

For macroscopic systems, the Coulomb coupling parameter is clearly defined by the condition that each particle occupies, on average a spherical volume (or, a circle in 2D) with the radius equal to b_{WS} . However, in this review we focus on finite 2D and 3D dust clusters in a (nearly) isotropic harmonic trap. Such systems have been studied for several decades theoretically and experimentally. Very good agreement has been found, in particular for two-dimensional finite systems. More recently also spherical 3D dust crystals could be produced [7], and their low-temperature structure is now well understood (for details see Sec. 2.1). For these finite systems with Coulomb or Yukawa interaction, Γ is still an appropriate qualitative measure for the coupling strength. Although these clusters have, in general, a spatially inhomogeneous density—due to formation of shells—and an average density decaying away from the center [8, 9], the average density can be approximated by the particle number N and radius of the outermost shell R_C . In experiments with finite dust clusters, Γ values of several hundreds are easily achieved, even at room temperature, as will be discussed in

Secs. 5 and 6. In particular, it may be surprising that, for dusty plasmas, the major challenge for many applications is to *lower the coupling strength*. The main task is to do this in a controlled manner by increasing only the dust temperature T_d , without affecting the other plasma parameters. This is particularly important in order to study the thermodynamic properties, the melting process and the different phases of these systems. To achieve a controlled heating of dust clusters several methods have been used, including variation of the rf power or the neutral gas pressure. However, these methods usually alter the whole discharge environment and, thus, effectively create a different plasma, making a “clean” analysis of dust thermal effects difficult [10, 11].

A suitable approach to heat the dust without affecting the discharge environment is the use of lasers. The control of matter by lasers has seen dramatic progress over the last two decades. This includes the manipulation of single large particles by using the intensity profile of a laser beam (“laser tweezers”) [12] or the trapping of atoms and molecules in the standing wave pattern of several lasers (optical traps or optical lattices) [13]. An alternative way to influence massive particles is to use the light pressure to transmit energy and momentum. The range of applications reaches from particle acceleration (laser wake field acceleration) [14] to heating of dense fusion plasmas with the help of extremely intense lasers, e.g. [15] and references therein. In similar manner, for dusty plasmas a focused low intensity laser beam is well capable to accelerate single particles. Similarly, stationary laser beams were used to excite shear flows in monolayer dust crystals [16, 17] or rotations in finite 2D clusters [18]. Mach cones could be excited by moving the laser spot through the cluster [19, 20]. A further application of moving laser spots is the realization of a thermal heat source for the dust component [21–23]. A more detailed description of these pioneering laser experiments is given in section 3.1.

In Kiel, Schablinski *et al.* applied the concept of moving laser spots to finite 2D dust clusters. As in the experiment of Nosenko and co-workers [16], a laser beam is split and the two beamlets are used to manipulate the cluster from opposite directions which prevents a net momentum transfer. Every beamlet is guided by a two-axis galvanometer mirror which allows for scanning virtually arbitrary patterns in the levitation plane. Since this heating scheme causes a higher temperature in beam direction than in the perpendicular direction, a second beam pair was added. Moreover, the scanning procedure was modified by introducing dynamically changed scanner frequencies. This setup is now applicable to adjust an isotropic 2D velocity distribution with increased dust temperature, see Sec. 5. A different heating scheme has been developed in Greifswald in order to manipulate finite 3D dust clouds. In this case, scanning the whole cluster volume homogeneously with three beam pairs—one pair for the x -, y -, and z -direction, respectively—is still beyond reach. Hence, one pair of heating lasers is used to manipulate the cluster from the horizontal direction. Each laser beam is rapidly moved to one position in the cluster and remains at this position for about one tenth of a second, accelerating dust grains during this time. Then, the rapidly moved to the next randomly chosen position via galvanometer mirrors [24].

The goal of this review article is to present an overview on these recent experimental developments, compare them to theory and to discuss possible future applications. We start by giving a brief overview on the properties of finite 2D and 3D dust clusters in Sec. 2. Then, we discuss the laser heating principle and how it is used to reduce the coupling strength in a controlled way (Sec. 3). Dedicated numerical simulations of the laser heating are presented in Sec. 4. Experimental results for finite 2D and 3D dust clusters are presented in Secs. 5 and 6. We conclude in Sec. 7 with an

outline of future applications, including spatially inhomogeneous plasmas and time-dependent processes.

2. Structural, thermodynamic and transport properties of finite dust clouds

2.1. Structural properties

The striking property of solid Yukawa clusters in 2D as well as in 3D is their well ordered structure. This structure and the loss of order with increasing temperature is accompanied by a sequence of phase transitions (or structural transitions) which are peculiar in finite systems [25, 26]. Details of these transitions are still open and of high interest for many finite size systems. They depend on the particular crystal structure which we, therefore, review in the following.

The screening effect of electrons and ions results in the screening parameter κ in the Yukawa-type pair-interaction potential of the dust particles

$$\Phi_Y(\vec{r}_i, \vec{r}_j) = \frac{Q_d^2}{4\pi\epsilon_0 |\vec{r}_i - \vec{r}_j|} \cdot e^{-\kappa|\vec{r}_i - \vec{r}_j|}, \quad (2)$$

where $\kappa = \lambda_D^{-1}$ is given by the inverse Debye length[‡]. Wake effects due to the streaming ions are neglected in the presented results. The Hamiltonian of the N particle Yukawa cluster (prior to laser manipulation) is given by

$$\mathcal{H} = \sum_{i=1}^N \frac{1}{2m} \vec{p}_i^2 + \sum_{i=1}^N \frac{m\omega^2}{2} r_i^2 + \sum_{i<j} \Phi_Y(\vec{r}_i, \vec{r}_j), \quad (3)$$

where the first term describes the kinetic energy, the second the confinement energy due to the harmonic trap and the last the mutual Yukawa interaction energy. In this model, all dust grains are assumed to be equal in mass m and charge Q_d .

Small 2D dust clusters typically consist of concentric rings. The core region of larger clusters with several hundred particles, in contrast, shows a hexagonal structure, like in infinite systems. This lattice has dislocations at the outer shells, where the circular boundary has to be matched [27].

Finite 3D dust clusters consist of spherical shells instead of rings. Due to their spherical shape, these crystals are called *Yukawa balls* [or *Coulomb balls*, when screening can be neglected]. This structure is reproduced in first-principle simulations—molecular dynamics (MD) or Monte Carlo (MC)—and has been investigated in detail for both Coulomb balls [28–30] and Yukawa balls [31, 32]. The general trend is that, with increasing screening parameter κ , more particles occupy the inner shells.

Recently, also several analytical theories for the shell structure in 3D have been developed. The *local density approximation* as a continuum theory accurately describes the mean density profile of the spherical clusters [8, 9], but it misses the formation of shells. The positions and the populations of the shells of Coulomb balls are well reproduced by a slightly modified version of the *hypernetted chain approximation* which can be adapted to particles interacting via a Yukawa potential as well [33–36]. Beyond the radial shell structure, 3D dust balls exhibit a well ordered

[‡] The Debye length $\lambda_D = \left(\frac{q_e^2 \bar{n}_e}{\epsilon_0 k_B T_e} + \frac{q_i^2 \bar{n}_i}{\epsilon_0 k_B T_i} \right)^{-1/2}$ incorporates screening of electrons and ions. q_e (q_i) is the electron (ion) charge, \bar{n}_e (\bar{n}_i) is the average electron (ion) density and T (T_i) is the electron (ion) temperature.

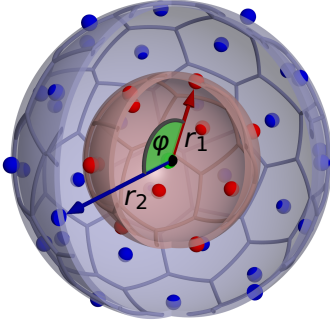


Figure 1. Yukawa ball with $N = 60$ particles consisting of two spherical shells and a single particle in the center. In order to sample the center-two-particle (C2P) distribution function based on the coordinates, for each particle pair, both radial coordinates r_1 and r_2 as well as the angular pair distance φ with respect to the trap center are recorded. The Voronoi grid of the intra-shell particle configuration is shown in gray.

intra-shell structure at strong coupling. In contrast to a flat 2D system, the spherical curvature requires a fraction of pentagonal Voronoi cells in the hexagonal pattern on the shell [30].

2.2. Thermodynamic properties and phase transitions

As the ground state properties of finite dust clusters are well understood by now [28–32], further investigations concentrate on thermodynamic properties at finite temperatures. When a cluster is excited by feeding thermal energy into the system, metastable states with energies above the ground state energy $E_0(N, \kappa)$ are occupied. These metastable states may differ from the ground state with respect to the occupation numbers of the shells or in the particle configuration within the shells. This “fine structure” [30] is observed for 3D but not for 2D clusters. The metastable states of Yukawa balls as well as their increased population with temperature were investigated in both experiment [37, 38] and first principle simulations [39, 40]. Among others, these simulations allowed to determine the barrier heights between different metastable states [39–41].

A remarkable feature of a phase transition in finite spherically confined dust clusters is the crossover from a well ordered structure with thin shells and a highly symmetric intra-shell order (3D), at low temperatures, towards a disordered particle fluid-like state, at high temperatures. Increase of temperature eventually results in melting which may involve a sequence of processes. In order to resolve these processes, the concepts for characterization of phase transitions known from macroscopic systems have to be re-considered and adapted. Hence, structural parameters are required to characterize the phase transition. While the heat capacity, i.e. the amount of heat δQ required per temperature increase δT to heat up the system, is a widely used melting parameter in solid state physics, measuring this parameter is challenging in dusty plasmas. The dust subsystem exchanges energy with electrons, ions and neutrals making it impossible to extract the pure heat capacity of the dust system with a particle number $N \lesssim 10\,000$ negligible compared to the number of the surrounding

plasma constituents [42]. In contrast, the pair distribution function and, even more, the center-two-particle distribution, discussed in the next section, have proven to be well suited for this purpose in theory as well as in experiments.

For the ring structure of 2D clusters, two different melting processes were identified. The first process is attributed to the rotation of one ring with respect to the other rings [18, 25, 43]. The required energy for such a rotation crucially depends on the exact occupation number of the rings. While the commensurate (“magic number”) $N = 19$ (1-6-12) configuration is very stable against inter-shell rotation, due to the matching particle numbers on the inner and outer shell, the $N = 20$ (1-7-12) configuration is extremely unstable against this excitation [18], i.e. it has a drastically reduced inter-shell rotation barrier and melting temperature. The second, radial melting process is attributed to particles undergoing a transition between two adjacent rings and, typically, takes place at substantially higher temperatures [10]. It is interesting to note that the same kind of two-stage melting process is observed in finite quantum clusters [44, 45], indicating that these are correlation effects which are of high interest also beyond the field of dusty plasmas.

The complexity of the melting process increases when advancing from 2D to 3D clusters [41, 46]. Besides the melting of the radial structure and inter-shell rotation, a third melting process is connected to the intra-shell order [46]. However, this classification should not hide the fact that the interplay between the melting processes is utmost complex and there is, in general, no separation of the different processes.

In order to trigger phase transitions in dust experiments, selective control over the dust kinetic temperature is essential. In particular, it is desirable to feed energy into the random dust motion without changing other plasma parameters such as the neutral gas pressure, the electron and ion temperatures and the flow velocity of the ions. A further requirement is that the entire cluster should be heated homogeneously while conserving the isotropic velocity distribution. As is described in the section 3, this selective control over dust temperature is possible by the means of strong laser light.

2.3. Key quantities for the analysis of finite dust clusters

An important structural parameter that characterizes the loss of order in extended systems is the *radial pair distribution function* $g(r_{ij}) = g(|\vec{r}_i - \vec{r}_j|)$. It is commonly defined by the average number of particle pairs found at a distance of r_{ij} divided by the number of pairs which one would find in a homogeneous (i.e. uncorrelated) system with the same density. An algebraic decay of the envelope of g over r_{ij} indicates a long range order in the solid regime. Moreover, the height of the first maximum allows to detect a melting line in the (Γ, κ) space [6]. For obvious reason, the long range behavior of the pair correlation function cannot be investigated for finite clusters.

The radial pair distribution function (average number of particle pairs with a distance in $[r_{ij}, r_{ij} + \Delta r)$ divided by the bin volume) drops to zero after a few nearest neighbor distances for finite clusters in both 2D and 3D, cf. Fig. 2 and Fig. 3, respectively. However, a fine splitting of the peaks in $g(r_{ij})$ is visible at high coupling strength indicating a frozen structure. When the temperature is increased, the subpeaks disappear. Finally, at a moderate coupling strength $\Gamma = 10$, the pair distribution function has only a single peak followed by a monotonous decay. The classification of inter-shell and intra-shell melting is not possible by means of this quantity as sampling the modulus of the distance does not distinguish whether the

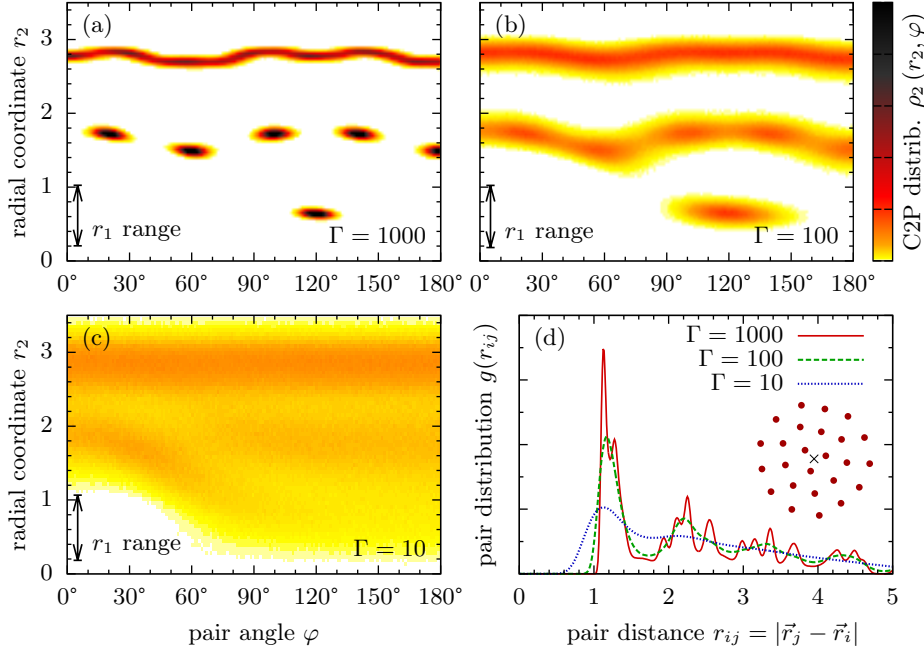


Figure 2. (a)-(c) Center-two-particle distribution function for a 2D Coulomb cluster with $N = 25$ particles for different coupling strengths. The ground state configuration consists of three concentric rings, see inset in (d). The first radial coordinate r_1 is integrated over a range corresponding to the inner shell indicated by the arrows. Intra-shell correlations are visible at $r_2 \sim 0.7$ and $\phi = 120$. Pronounced inter-shell correlations with particles on the second shell are found at $r_1 \sim 1.6$ for strong coupling. (d) The radial pair distribution function $g(r_{ij})$ shows distinct peaks at high Γ which vanish when Γ is being decreased. Note that $g(r_{ij})$ decays to zero for all couplings, due to the finite size of the cluster. Results are from a Monte Carlo simulations, Γ is defined with the length unit $r_0 = [Q_d/(4\pi\epsilon_0 m\omega)]^{1/3}$ as characteristic pair distance.

particles of a pair are on one shell or on different shells.

For this reason, the *center-two-particle* (C2P) distribution function $\rho_2(r_1, r_2, \varphi)$ is introduced which takes into account the radial position of both particles as well as their angular distance with respect to the trap center [24, 47]. A sketch of the sampled coordinates is shown in Fig. 1 for a 3D Yukawa ball consisting of two spherical shells and one particle in the center. Since $\rho_2(r_1, r_2, \varphi)$ is invariant under rotation of the entire cluster, it is not necessary to remove a rigid rotation before sampling. Integration of ρ_2 in both radius coordinates over a range corresponding to one shell allows to extract the angular pair distribution function within that shell. When only one radius coordinate is integrated, $\rho_2(r_1, \varphi)$ can be plotted in a color map, as is done for a 2D cluster, in Fig. 2, and a 3D cluster, cf. Fig. 3. In this color map, the intra-shell structure is responsible for the peaks in φ -direction. Moreover the radial density is also included in this quantity in form of the radial extension of the colored area. While the given data are from MC simulations, equally well one can use experimental data, cf. Fig. 12.

For the 2D cluster with $N = 25$ particles, a reference particle from the inner shell

is chosen by the integration range around $r_1 \approx 0.7$. Since the inner shell consists of three particles, the intra-shell neighbors appear as a peak at $\varphi = 120^\circ$. At $\Gamma = 1000$, the distinct peaks found around $r_2 \approx 1.6$ show that the angular orientation of the second shell with nine particles is locked with respect to the inner shell. This inter-shell order disappears between $\Gamma = 1000$ and $\Gamma = 100$ where ρ_2 is smeared out in angular direction. At moderate coupling, $\Gamma = 10$, hardly any angular correlations remain and also the radial order is lost. Particle transitions between different shells are revealed by a finite density in the radial regions between the shells.

For strong coupling, the 3D Yukawa cluster with $N = 60$ particles is found in a configuration which has one particle in the center, 15 particles on the inner shell and 44 particles on the outer shell (44-15-1). Again, one reference particle is chosen from the inner shell by integrating over r_1 . Due to the complexity of the particle composition on a spherical shell compared to the composition on a ring in 2D, the peaks at $r_2 \approx 1.2$, indicating intra-shell correlations, are not as sharp as for the 2D cluster at high coupling. Inter-shell correlations appear as dark and bright areas in the horizontal stripe at $r_2 \approx 2.4$. This radius corresponds to the outer shell. At moderate coupling, $\Gamma = 10$, the angular correlations are lost and frequent transitions between the shells take place as seen by the radial extension of the density. Note that a high density is found around $\varphi = 90^\circ$ and the general trend of ρ_2 is to increase with r_2 . These two trends in 3D are attributed to the spatial volume contributing to each point which scales as $V_{\text{bin}} \propto r_1 \cdot r_2 \cdot \sin(\varphi)$. In contrast, the volume element is independent of r_1 , r_2 and φ in 2D.

2.4. Transport properties

Besides thermodynamic properties, also transport coefficients and their dependence on parameters like temperature or the magnetic field strength are important characteristics of dusty plasmas. A particularly important example of transport coefficients is the diffusion coefficient. Diffusion was investigated in detail in macroscopic systems, e.g. [48, 49] and references therein. In particular, in two dimensions an anomalous diffusion was found [50–52] which turned out to be a transient effect [53]. Furthermore simulations were performed for magnetized dusty plasmas. Here, the diffusion coefficient D_\perp perpendicular to the magnetic field as well as the parallel diffusion coefficient D_\parallel were found to be strongly affected by the magnetic field in the strong coupling regime approaching Bohmian diffusion (decay with B^{-1}) [49]. Recently diffusion in a two-dimensional one- and two-component magnetized strongly coupled plasma was studied and interesting behavior of the diffusion coefficients of both components was reported [54].

One way to compute (or measure) the diffusion coefficient in a macroscopic system is to use the mean square displacement (MSD)

$$u_r(t) = \left\langle |\vec{r}(t) - \vec{r}(t_0)|^2 \right\rangle_N = 2 \dim Dt^\alpha, \quad (4)$$

as an average over all N particles. Here \dim is the system dimensionality (2 or 3) and α is the diffusion exponent which equals one for normal diffusion. However, the long time behavior of the MSD has only limited meaning for mesoscopic systems since there the particles reach the cluster border after a few inter-particle distances [55].

Therefore, a different method is required to calculate the diffusion coefficients in small clusters. The instantaneous normal mode (INM) analysis has proven successful to this purpose [56–61]. This method deduces dynamic properties of a liquid state

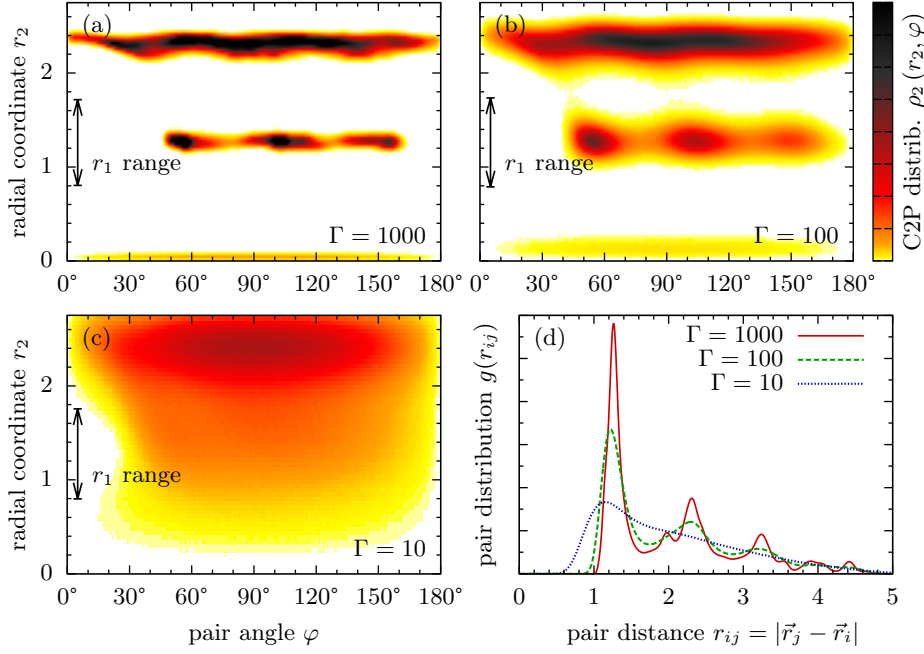


Figure 3. (a)-(c) Center-two-particle distribution function for a 3D Yukawa ($\kappa = 1$) ball with $N = 60$ particles for different coupling strengths. The ground state configuration consists of two concentric spherical shells and one particle in the center. The first radial coordinate r_1 is integrated over a range corresponding to the inner shell (arrows). *Intra-shell* correlations are visible at $r_2 \sim 1.3$. *Inter-shell* correlations with particles on the outer shell are visible at $r_1 \sim 2.2$ by the angular modulation of $\rho_2(r_2, \phi)$. (d) The radial pair distribution function $g(r_{ij})$ shows distinct peaks at high Γ which vanish when Γ is being decreased. Note that $g(r_{ij})$ decays to zero for all couplings, due to the finite size of the cluster. Results are from a Monte Carlo simulations, Γ is defined with the length unit $r_0 = [Q_d/(4\pi\epsilon_0 m\omega)]^{1/3}$ as characteristic pair distance.

from the curvature of the energy landscape of the momentary configuration of the cluster. The first step is to calculate the dynamical (Hessian) matrix of the potential energy in the Hamiltonian, Eq. (3), as

$$\mathbf{A} = \left(\frac{\partial^2 E}{\partial r_{i\alpha} \partial r_{j\beta}} \right), \quad (5)$$

where i, j are particle indices and α, β indicate the (two or three) components of the coordinates. The eigenvalues of this matrix present the squared eigenfrequencies ω_l^2 of the system. In a stable state, all these eigenvalues are positive resulting in real eigenfrequencies which reflect stable oscillations around the particles' equilibrium positions. A liquid instantaneous configuration, in contrast, has also negative eigenvalues of \mathbf{A} , resulting in purely imaginary eigenfrequencies reflecting unstable modes.

The second step is to calculate the spectral density, $\rho(\omega)$, which is normalized to unity, $\int d\omega \rho(\omega) = 1$. In turn, we average over the normal modes of many

configurations

$$\rho(\omega) = \left\langle \sum_{l=1}^{\dim \cdot N} \delta(\omega - \omega_l) \right\rangle. \quad (6)$$

This density is composed of a stable part $\rho_s(\omega)$, with real frequencies, and an unstable part $\rho_u(\omega)$, with imaginary frequencies. The unstable part $\rho_u(\omega)$ is associated to a negative curvature in the momentary potential landscape. As described in Refs. [56–61], especially $\rho_u(\omega)$ can be related to the diffusion constant. The self diffusion constant is expressed as [56–61]

$$D = \frac{k_B T}{m} \int \rho(\omega) \frac{\tau_h}{1 + \tau_h^2 \omega^2} d\omega. \quad (7)$$

It depends on the temperature $k_B T$, the particle mass m and the average “hopping time” τ_h for the transition across potential barriers between two local potential wells. This time is known as the inverse hopping frequency and calculated as

$$\tau_h^{-1} = c \int \frac{\omega}{2\pi} \rho(\omega) A \exp\left(-B \frac{\omega^2}{k_B T}\right) d\omega, \quad (8)$$

where $c \approx 3$ is constant taking into account the different routes to escape from a local potential minimum and the constants A and B are obtained from an exponential fit of $\rho_u(|\omega|)/\rho_s(\omega)$. For details, we refer the reader to Refs. [56–61].

3. Controlled change of the coupling strength by laser manipulation

3.1. General concept

In order to obtain valid information on thermodynamic properties it is essential to gain reliable control on the coupling parameter of the system. According to Eq. (1), three possibilities exist to control Γ : (i) controlling the charge Q_d of the particles, (ii) controlling the inter-particle distance b_{WS} , and (iii) controlling temperature T . With $\Gamma \sim Q_d^2$, already a moderate variation of charge allows to change the coupling strength considerably. Thus, controlling the charge on the particles is the most tempting approach. However, this is practically not feasible. Q_d is determined by geometric properties of the particles and by the plasma conditions in the vicinity of the particles. Except for rare special conditions, the geometric properties cannot be altered during experiments and the local plasma conditions are not solely set by the discharge parameters but are modified by neighboring particles as well. Thus, the charge is not directly controllable by means of external parameters such as discharge power, neutral gas pressure or bias voltages. Each, will affect the plasma as well as the particle arrangement and thus result in a rather complex parameter dependence. Especially the inter-particle distance is strongly determined by the mutual particle repulsion, i.e. the particle charge, and the external confinement. Thus, there is no easy access to control charge and inter-particle distance independently.

Therefore, to increase the coupling strength, temperature is the only remaining control parameter. Due to the macroscopic size of the particles two temperatures have to be distinguished: The kinetic temperature of the particles and the particle surface temperature. For Γ only the kinetic temperature is of interest. Usually we find in experiments that the kinetic temperature of the particles is significantly higher than their surface temperature. Therefore, the kinetic temperature cannot be obtained from a conventional heat flux analysis. Recent investigations by Fischer *et al.* [62] state that

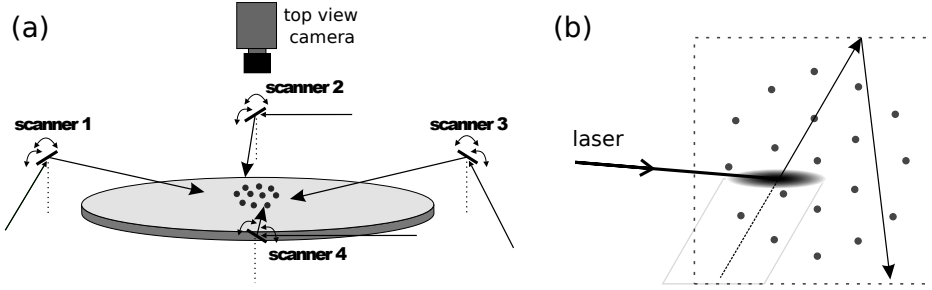


Figure 4. (a) Setup for a laser heating experiment using 4 laser beams. The spot of each laser beam is moved through the plasma crystal's layer by independently controlled scanning mirrors. The scanned area is large enough to cover the entire crystal. The radiation pressure force impels the particles in \vec{e}_{\parallel} direction. (b) The improved heating method moves the spot with constant speed in both directions until the border of the scanned area is reached. At this point, a new speed is chosen randomly for the inverse direction.

electrostatic fields in the plasma background provide a significant contribution to the kinetic temperature of dust particles. However, a basic understanding of the involved processes is still missing and this makes it difficult to control temperature this way.

Nevertheless, there is an alternative approach to control the kinetic temperature. Temperature is a process where random collisions of particles finally result in a Maxwellian velocity distribution. Fortunately, it is not important how this Maxwellian velocity distribution is generated. Thus, a thermostat for dust particles should simply use a random force to drive particles and use collisions to thermalize, i.e. yield the desired velocity distribution. Such a driver can be provided by strong laser light. Light scattering implies a momentum transfer to the particles. Combined with the small weight of the particles and low friction, these laser beams are capable to accelerate dust particles. A true thermostat based on such a laser manipulation would produce a spatially homogeneous momentum transfer with random direction and strength for every particle.

The idea to transfer momentum from a laser beam to a dust particle goes back to the early days of dusty plasma research [63–68] and has been used for many purposes so far, e.g. investigations of particle interaction potentials [69–71], driving waves [64, 67], investigate Mach cones [19, 20, 72, 73], stability and mode analysis [18]. The first systematic laser heating experiments were performed by Wolter *et al.* [21] and by Nosenko *et al.* [22, 23]. Their experimental setup used two opposing laser beams which were directed to a 2D plasma crystal. The positions of the laser beams are controlled with scanning mirrors. Using Lissajous figures with an irrational frequency ratio a well defined area of the plasma crystal is scanned, i.e. heated. In addition, the opposing beam setup assures that the average transferred momentum cancels while the kinetic energy of each particle is raised. Nosenko *et al.* showed that their laser heating results in a Maxwellian velocity distribution parallel and perpendicular to optical axis. However, the temperature in perpendicular direction was found significantly lower. Obviously, the viscous damping of the neutral gas impedes that collisions redistribute sufficient energy in perpendicular direction.

To overcome this limitation recent laser heating experiments for 2D clusters use four laser beams, where each optical axis is equipped with two opposing beams and

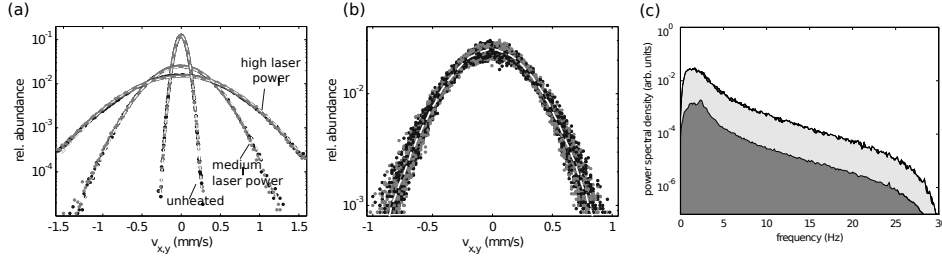


Figure 5. (a) Average particle velocity distribution function for a cluster of 19 particles for different heating power. The velocity components in x and y direction (gray and black dots) are plotted separately. For each case (unheated, medium and high heating power) Gaussian fits (white dashed lines) indicate only slight deviation of an ideal Maxwell distribution. (b) velocity distributions for a heated system (similar to (a)), but here the distribution is calculated for each particle independently. The small scatter shows that all particles are heated equally. (c) the power spectrum of the velocity fluctuations. The spectrum of the unheated system is plotted in dark gray. The spectra of the x and y component of a heated system are plotted (light gray and black). Note that both components are equally heated and no artefacts from the scanning process can be found in the spectra.

perpendicular orientation of both optical axes [74, 75], see Fig. 4(a). In addition, the scanning procedure has been optimized. The reason for this is that a scanning scheme based on Lissajous figures results in a velocity power spectrum where strong harmonics of the scanning frequencies are observed. This is an indication that the periodicity of the driver causes individual particles to move with the same periodicity, i.e. between two kicks of the laser the particle velocity decreases significantly. Therefore, the optimized scanning procedure (see Fig. 4(b)) assures that each particle is driven by a laser beam before its motion originating from the previous laser drive is damped out. Thus, the requirement that each spatial position is covered by the scanning procedure is only sufficient if the maximum time between two complete scans is less than the inverse of the damping rate. The experiments of Schablinski *et al.* demonstrated that this is feasible for small clusters ($N < 100$). Their measured velocity spectra show no remaining peak of the scanning lasers. Fig. 5 summarizes the basic features of their heating method. In Fig. 5(a) the velocity distributions of the heated system are clearly Maxwellian. Plot (b) stresses that the Maxwellian character is even obtained if the velocity distribution is checked for each particle individually. The small scatter in particle temperature is a clear indication that the heating process is spatially homogeneous. Therefore, the laser heating with four laser beams and an optimized scanning procedure can be regarded as an ideal thermostat for dusty plasma crystals.

4. Numerical simulation of 2D laser heating

In this section, we describe how the 2D laser manipulation experiment with the elaborate heating scheme presented in Sec. 5 is simulated with a Langevin molecular dynamics (LMD) method [74–76]. The purpose of these simulations is to suggest optimal values for the heating parameters and future experiments like inhomogeneous heating. Moreover, computer simulations provide the possibility to scan single parameters like the heating power or the beam (spot) size at constant other

parameters. In an LMD simulation, the Langevin equations of motion for the dust component

$$m \frac{d\vec{v}_i}{dt} = \vec{F}_i - \gamma m \vec{v}_i + \vec{\xi}_i(t), \quad (9)$$

for all dust grains i are integrated numerically. In these equations, one contribution to the acceleration of a dust particle on the left hand side is the same force term \vec{F}_i as in Newton's equation of motion which results from the Hamiltonian, Eq. (3). The last two terms on the right hand side describe the frequent collision of the dust grains with the neutral gas background statistically by a viscous damping force, $-\gamma m \vec{v}_i$, and a random force $\vec{\xi}_i(t)$. The random force has zero average and can be modeled by a Gaussian probability distribution with correlation function

$$\langle \xi_{i,\alpha}(t) \xi_{j,\beta}(t') \rangle = 2\gamma m k_B T \delta_{i,j} \delta_{\alpha,\beta} \delta(t - t'), \quad (10)$$

where i, j are particle indices and $\alpha, \beta \in \{1, 2\}$ subscript the spatial direction of the random force vector. The amplitude of this force depends on the temperature $k_B T$ as well as on the friction coefficient γ via the fluctuation-dissipation theorem.

As described in the introduction, electrons and ions screen the repulsive interaction of the dust grains. Therefore their interaction is described by a Yukawa potential, Eq. (2). In experiments on 2D clusters, the strong vertical confinement in the plasma sheath allows the formation of monolayer clusters. Therefore, the system is treated strictly two-dimensional in the simulation.

The dominating effect of every single heating laser beam is a momentum transfer by the radiation pressure. If the spot hits a dust grain, this grain is accelerated in beam direction. As sketched in Fig. 4, the laser beams strike the cluster from above the levitation plane with a low angle of incidence. The out-of-plane component of the accelerating force is considered to have no impact on the particles motion due to the strong vertical confinement. However, the spot profile is stretched in beam direction due to the angle of incidence $\alpha < 90^\circ$. The effect of the laser spots is included in the equations of motion, Eq. 9, as an additional time and space dependent force. The amplitude of the force depends on the particle's position inside the spot which is described by an anisotropic Gaussian intensity profile. The force acting on a particle at position $\vec{r} = (x, y)$ is described by

$$\vec{f}_l(\vec{r}, t) = \frac{P_0}{2\pi\sigma_x\sigma_y} \cdot \exp\left[-\frac{(x - x_l(t))^2}{2\sigma_x^2} - \frac{(y - y_l(t))^2}{2\sigma_y^2}\right] \vec{e}_l, \quad (11)$$

where $\sigma_{x,y}$ characterizes the spot profile and \vec{e}_l is the beam direction. The amplitude of the force P_0 is determined by the laser power, the cross section of the dust grain and its absorption and reflection characteristic. Since only the in-plane component has an effect on the the particle's motion, P_0 is reduced by the factor $\cos \alpha$ where α is the angle of incidence. The trajectories within the levitation plane $\vec{r}_l(t) = (x_l(t), y_l(t))$ of the different spots l depend on the heating scheme.

All three investigated heating methods use triangular signals to drive the x - and y -oscillations of the lasers spots $x(t) = x_0 \cdot \text{triag}(f_x t)$, $y(t) = y_0 \cdot \text{triag}(f_y t)$. Using a sinusoidal signal would cause an increased intensity at the borders of the scanned area. The heating methods differ in the scanning frequencies f . These frequencies are fixed for heating methods A-I. Method A-I uses the same frequencies for both laser and a pseudo-irrational ratio f_x/f_y . For method B, the scanning frequencies are dynamically changes each time a laser spot reaches the border of the scanned area.

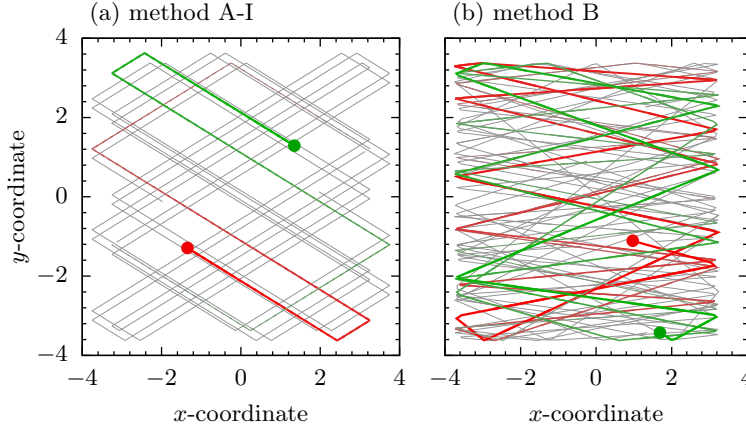


Figure 6. Trajectories of the laser spots (red/green: $\pm x$ -direction) for the three investigated heating methods. (a) Method A-I uses a pseudo-irrational frequency ratio. (b) Using method B, a new scanning frequency is randomly chosen each time a laser spot reaches the border. Here, the additional spots in $\pm y$ -direction are omitted for the sake of clarity.

method	A-I	B
laser beams	2	4
frequency ratio	pseudo-irrational	random frequencies
f_{\parallel}	14.5623 Hz	50–300 Hz
f_{\perp}	9.0 Hz	15–60 Hz

Table 1. Parameters defining the pattern which is scanned by the lasers. Since both beams are oriented in $\pm x$ -direction for methods A-I, $f_{\parallel} = f_x$ in that case.

Hence, no pattern is repeated. Moreover, a second pair of lasers accelerating particles in y -direction is added [74, 75]. The parameters of all heating methods are summarized in table 1 and the scanned patterns are shown in figure 6.

For the simulation results presented in this review, we used $r_0 = (Q_d^2/(4\pi\epsilon_0 m\omega^2))^{1/3}$, $t_0 = \omega^{-1}$, and $E_0 = (Q_d^4 m\omega^2/(4\pi\epsilon_0)^2)^{1/3}$ as dimensionless units for length, time and energy, respectively. For the numerical integration of the stochastic differential equations, we used an integration scheme described by Mannella *et al.* that can be considered as an extension of the “leap frog” scheme [77]. For details concerning the simulations, we refer the reader to Refs. [75, 76]. The integration scheme can also be generalized to incorporate homogeneous magnetic fields of arbitrary strength [78–80].

The LMD simulations confirmed the importance of randomly changing the scanner frequency. Especially rational scanning frequency ratios f_x/f_y which result in a closed scanning pattern prove to be problematic.

The excellent heating qualities with respect to homogeneous heat input of the random frequency method B were confirmed in LMD simulations [75]. The second beam pair in y -direction turned out to be essential in order to achieve an isotropic heating effect. While constant scanning frequencies and combinations of them appear as peaks in the power spectral density (PSD) of the particle velocities, this artefact

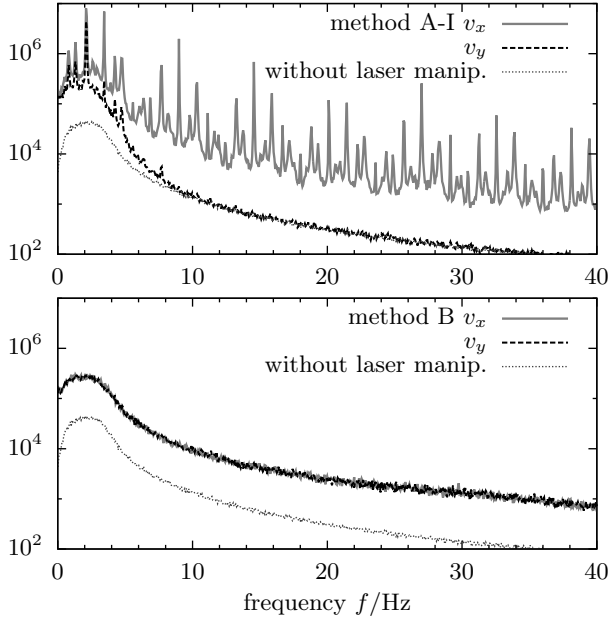


Figure 7. Power spectral density (PSD) of the dust velocity averaged over all particles of a Yukawa cluster with $N = 38$ particles with different heating methods (trap frequency $\omega = 5.5 \text{ s}^{-1}$). **Top:** Method A-I uses one pair of laser beams in $\pm x$ -direction and a pseudo-irrational scanning frequency ratio f_x/f_y . **Bottom:** Heating method B uses two pairs of laser beams to accelerate the particles in both $\pm x$ - and $\pm y$ -direction. The scanning frequencies are randomly chosen each time the border of the scanned area is reached. The spectra for v_x and v_y coincide, here. Only this method conserves the shape of the PSD by shifting the entire spectrum to higher energies.

is removed by randomly changing the scanning frequencies, see Fig. 7 and Fig. 5(c). The PSD further discloses that effective energy transfer from x - to y -motion works for low frequencies, $f \lesssim 8 \text{ Hz}$, only. The pseudo-irrational frequency method A-I shifts the entire spectrum of the motion in x -direction to higher energies but also induces several peaks at the scanner frequencies and combinations of them, Fig. 7(a). Both experiment, Fig. 5(c), and LMD simulation, Fig. 7 (bottom), show that the random frequency method B is well suited as a thermostat for the dust system. The energy input is homogeneous over the entire frequency spectrum. It is also homogeneous in space and the Maxwellian shape of the velocity profile is conserved in both x - and y -direction.

Moreover, the random frequency method B is very robust against changes in the laser parameters [75]. The temperature increases ΔT —the heating effect—is reduced when the typical scanning frequency \bar{f} of the laser beams is increased as $\Delta T \propto \bar{f}^{-1}$. Having this relation in mind, only a low scanning frequency is favorable. However, in order to achieve a thermal heating effect, each particle should frequently be affected by a laser spot. This condition is violated for \bar{f} below the trap frequency ω . Therefore, scanning frequencies of the order of a few ω are advantageous [75].

5. Experimental results for 2D clusters

As already mentioned, there have been several investigations where laser manipulation and laser heating have been used to investigate the dynamics of 2D plasma crystals and liquids. This section will concentrate on finite 2D clusters and their thermodynamic properties. Especially the phase transition of these small systems is of interest as it should significantly depend on the cluster size. The following experiments use the isotropic heating method B of Schablinski *et al.* [74, 75], which has been introduced in the previous section. The laser heating provides a heat bath for the dust particles and the dust system is in thermodynamic equilibrium. Changing the laser power will result in a different temperature of the heat bath. For each temperature, long time series are recorded to obtain the trajectories of all particles. Examples of such particle trajectories are shown for low, medium and high temperature in Fig. 8(a). For low temperature the particles are well localized and only a slight angular rotation is observed. At medium temperature the particles are less localized in angular direction. Finally, the radial correlation vanishes at high temperatures. Thus, the melting process has two phases: first a loss of angular correlation and second a loss of radial correlation [81].

To determine the melting temperature several methods have been proposed (see [82] and references therein). Unfortunately most of them either fail for small clusters or are experimentally not feasible due to extremely long time series for sufficient statistics, see Sec. 2.2. Therefore, recently different methods have been applied which were introduced in Secs. 2.3, 2.4: The first is the Instantaneous Normal Mode (INM) analysis. This method computes the frequencies of the eigenmodes of a cluster from the eigenvalues of the dynamical matrix, see Sec. 2.4. The results of such an INM-analysis are plotted in Fig. 8. The plots show that, above a critical temperature, the diffusion constant increases linearly with temperature. A freezing temperature can be derived approximately from the point where D vanishes [83]. Thus one can estimate a melting temperature T_M by extrapolating the $D(T)$ curve toward zero. Especially in Fig. 8(b) the comparison of a highly symmetric cluster ($N = 19$) and a cluster with low symmetry ($N = 20$) reveals that the melting temperature of the symmetric cluster is significantly higher ($T_M^{19} \approx 9.000$ K, $T_M^{20} \approx 2.000$ K). A systematic investigation of melting temperatures as a function of particle number [61] has shown that symmetry has a mayor influence on melting temperatures of finite systems, confirming earlier theoretical predictions [25, 45].

The above results show that the INM analysis is sensitive to the cluster symmetry. However, it does not resolve different melting processes such as inter-shell and intra-shell melting. For this reason, we also consider the center-two-particle distribution [Sec. 2.3] for the experimental 2D cluster. Fig. 9(a) shows a highly ordered structure of the weakly manipulated cluster. The inner shell is occupied with six particles. Intra-shell neighbors are found under angles of $\varphi = 60^\circ$, 120° and 180° , resulting in clear peaks at these angles and a radius $r_2 \approx 1\text{mm}$, corresponding to the inner shell. The outer shell is occupied by twelve particles and the angular order with respect to the inner shell is fixed. Distinct peaks are visible at multiples of $\varphi = 30^\circ$. When the laser power is increased to a moderate value (cf. Fig. 9(b)), clear intra-shell and inter-shell correlations persist. However, inter-shell rotation (“angular melting”) has started, as the peaks at the outer radius are no longer fully separated. At the inner shell radius, weak peaks at $\varphi \approx 103^\circ$ and $\approx 154^\circ$ (arrows in Fig. 9(b)) indicate the occurrence of configurations with seven particles on the inner shell. The appearance

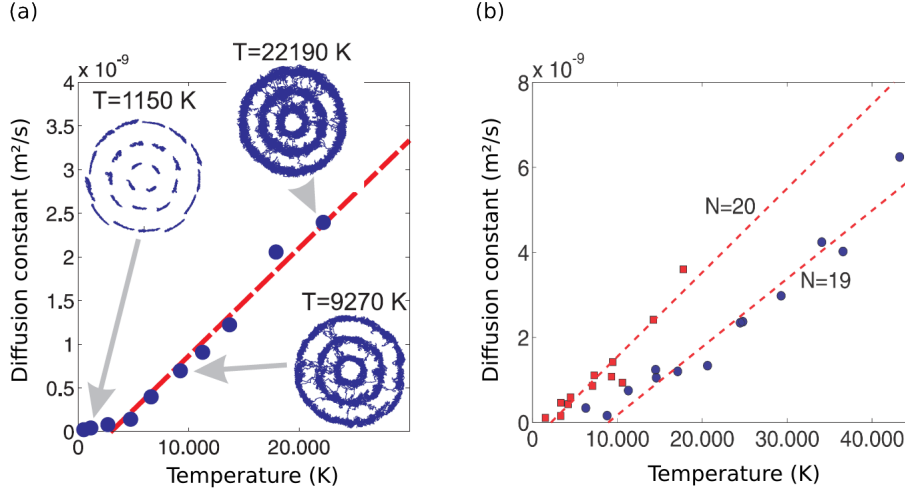


Figure 8. Diffusion constant as a function of temperature for finite 2D clusters. (a) Above a critical temperature the diffusion constant increases linearly with temperature. The insets show trajectories of a dust cluster with $N = 26$ particles at different temperatures. (b) Diffusion constant for two different dust clusters. The $N = 19$ cluster with its (1-6-12) shell occupation is highly symmetric, and its critical temperature is significantly higher than that of the less symmetric $N = 20$ cluster. (From Ref. [61]).

of this metastable configuration indicates the onset of radial melting. Finally, at high laser power (Fig. 9(c)), the correlations between inner and outer shell have vanished almost completely. At this heating power, the frequent particle transitions between the two shells give rise to a finite density in the region between these shells. The C2P distribution function confirmed the stability of this “magic number” cluster against inter-shell rotation. The quantitative analysis of the different melting temperatures and their dependence on the particle number is still outstanding.

6. Experimental results for 3D clusters

Three-dimensional dust clusters are formed in parallel plate radio-frequency (rf, 13.56 MHz) discharges, see Fig. 10. The discharges are typically operated in argon at gas pressures between 1 and 100 Pa and at rf powers between 1 and 10 W. The dust grains trapped in the discharge generally are monodisperse plastic microspheres with diameters chosen between 3 and 10 μm . These three-dimensional clusters are trapped inside a cubic glass cuvette placed onto the lower electrode. The glass box provides inward electric forces on the negative dust grains. To compensate the gravitational force an upward thermophoretic force is applied by heating the lower electrode. The combination of all forces provides a 3D harmonic confinement [84]. There, the particles arrange in nested spherical shells forming Yukawa balls or Yukawa clusters [7, 37, 85], cf. Sec. 2.1.

In the experiments described here, the particles are illuminated by low-intensity laser beams and the scattered light is recorded with high-speed video cameras at frame rates of 50 to 200 frames per second (fps), typically [24, 37, 85, 86]. For the observation of the 3D clusters a stereoscopic camera setup [37] is used where the

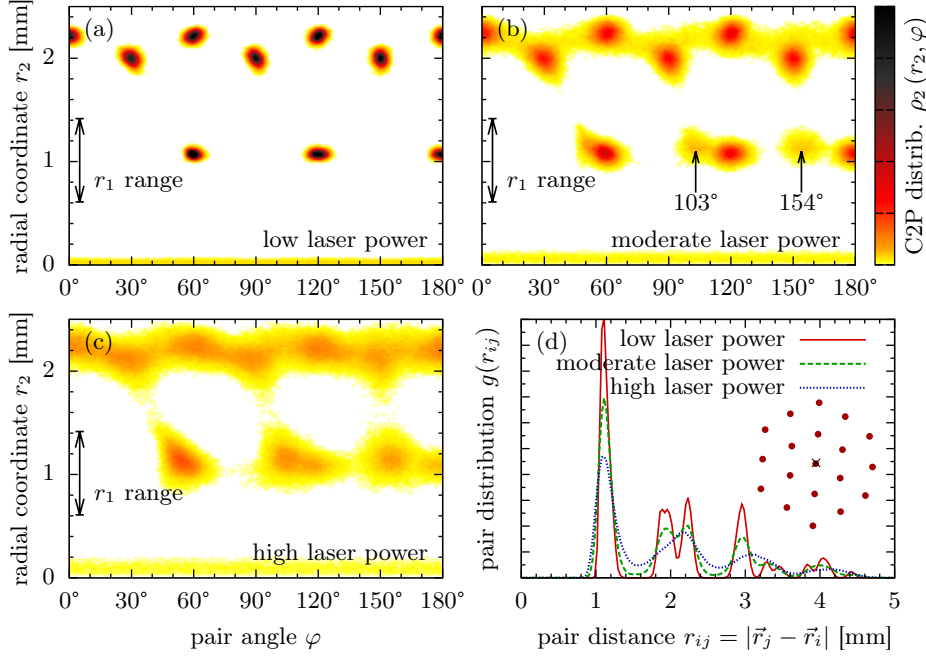


Figure 9. (a)-(c) C2P distribution function for a laser heated cluster of $N = 19$ particles. The low laser power corresponds to $T=2.800$ K, the moderate laser power corresponds to $T=17.000$ K and the high laser power corresponds to $T=34.000$ K. The first radial coordinate is averaged over the inner shell (arrow). (d) The radial pair distribution function for all three laser powers does not distinguish between different shells. The inset shows the cluster configuration at the lowest laser power.

particles are observed from three orthogonal directions. This setup allows to measure and reconstruct the full 3D trajectories of clusters with up to $N = 100$ particles with high temporal resolution [37, 87]. Consequently, the dynamical properties of the dust cluster can be followed for all particles individually. To realize a heating process for these 3D clusters a simpler approach than for the 2D case had to be chosen. Here, two additional opposing laser beams are oriented parallel to the electrode and are randomly swept over the cross section of the cluster with a dwell time of $\tau = 0.1$ s at each position [24, 86, 88]. The two laser beams at 660 nm wavelength are operated with up to 1 W output power. The random “kicks” to the particles by the radiation pressure mimic a heating process for these 3D clusters. The transfer of the elaborate heating schemes used for the 2D clusters to the 3D case would require six beams, two of which would be blocked by the electrodes.

As a consequence, the resulting velocity distribution of the particles in the cluster is only near-Maxwellian, with an overpopulation of “cold” dust particles [24]. Also the heating is more effective in the direction of the beams resulting in higher temperatures along this axis. Consequently, this laser-heating scenario of 3D clusters does not provide a true thermodynamic heating, yet. Nevertheless, from the velocity distributions reasonable kinetic temperatures $kT_\alpha = m\langle v_\alpha^2 \rangle$ with $\alpha = x, y, z$ can be assigned and temperatures of the order of a few times 10^4 K (few eV) have been

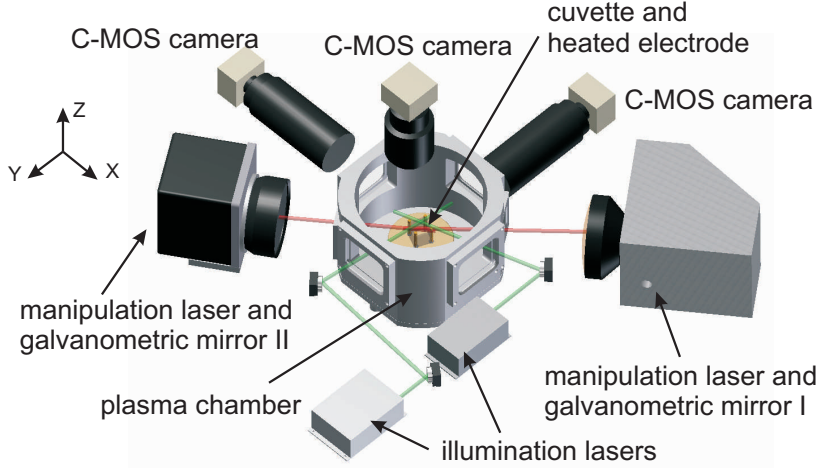


Figure 10. Sketch of the experimental setup. The particles are trapped in the cubic glass box and are illuminated by two Nd:YAG lasers from two sides and heated by two diode lasers from opposite directions. The three orthogonal high-speed cameras allow to trace the full 3D particle motion individually. (From Ref. [88].)

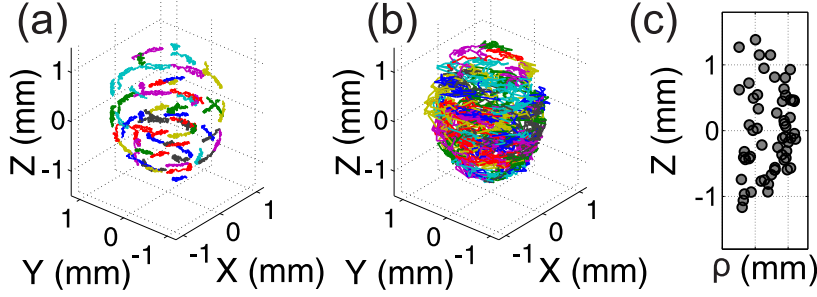


Figure 11. Trajectories of a $N = 60$ particle cluster recorded over a time span of about 10 s. (a) Without laser excitation, (b) with 250 mW laser power. (c) Equilibrium particle positions in cylindrical coordinates $\rho = \sqrt{x^2 + y^2}$ and z for the unheated case (a). (From Ref. [88].)

realized by this laser heating setup.

Here, as an example, the heating and melting of a 3D cluster with $N = 60$ particles is demonstrated§ using the pair of opposing heating laser beams. The Yukawa ball is spherical in shape and consists of two shells, see Fig. 11. By increasing the laser power, the amount of heating is increased and melting is achieved. For low laser heating power the cluster remains in a solid-like arrangement, as seen from the particle trajectories. Stronger random particle motion is excited at higher laser power where then frequent intra-shell and inter-shell particle exchanges are seen. Hence, the cluster is apparently driven into the liquid regime. The change of structural and thermodynamic properties

§ This cluster is formed from $4.86 \mu\text{m}$ particles at a gas pressure of 6.4 Pa and at a rf power of 1.3 W.

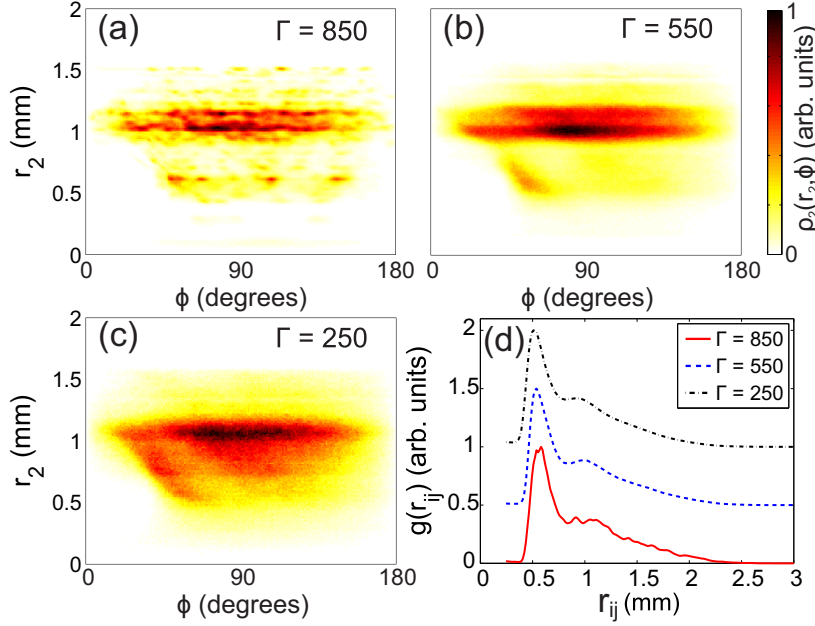


Figure 12. Center-two-particle distribution functions for the $N = 60$ cluster, a) without laser heating ($\Gamma = 850$), b) for a laser heating power of 100 mW ($\Gamma = 550$) and c) 300 mW ($\Gamma = 250$). d) Pair distribution function. The smoothening of the curve with decreasing Γ indicates the loss of order but, in contrast to the C2P distribution function in a)-c), the pair distribution function cannot distinguish intra-shell from inter-shell correlations. (The zero line is shifted for $\Gamma = 550$ and $\Gamma = 250$, for sake of clarity.)

that is induced by the lasers is illustrated in Fig. 12(d). There we show the pair distribution function $g(r_{ij})$ for three different heating powers. The differences in $g(r_{ij})$ between the three heating powers are only small. All three curves show a pronounced first-neighbor maximum at $r_{ij} \approx 0.6$ mm, a shoulder at $r_{ij} \approx 1.2$ mm corresponding to second neighbors and a decay to zero. While the curves for $\Gamma = 250$ and $\Gamma = 550$ appear smooth, a substructure is visible at high coupling, $\Gamma = 850$. The loss of order is reflected more clearly in the C2P distribution function.

As for the 2D case, the C2P distribution function allows to quantitatively assess this melting transition for these 3D clusters, see Fig. 12. There, these distribution functions are shown for a cluster with and without laser heating. As for the 2D case, one sees pronounced peaks at distinct angles φ and radii r_2 at low heating powers and subsequent loss of correlations for increased heating (reduced Γ). Also, in these 3D systems, laser heating provides a near-equilibrium heating scenario. A two-step melting (orientational melting before radial melting) which is expected for finite clusters [25, 43, 46, 89] is experimentally identified also for 3D clusters [24].

Finally, as another example of a liquid state property, the diffusion constant D , Eq. (7), has been derived from the 3D particle trajectories of the $N = 60$ cluster. The diffusion constant has been obtained from an analysis of unstable normal modes [61, 81, 86], see Sec. 2.4 above. The so obtained diffusion coefficient is shown in Fig. 13. For comparison also the diffusion of clusters of different sizes are also added

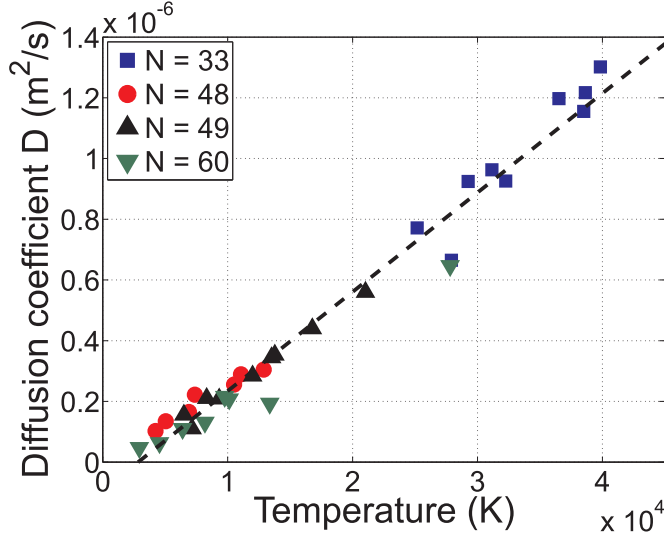


Figure 13. Diffusion coefficient $D(T)$ as a function of temperature for Yukawa balls of different size determined from an INM analysis. The dashed line corresponds to a linear fit to the diffusion coefficients for all clusters. (From Ref. [86].)

[86]. A linear relationship between diffusion coefficient and temperature is found for all studied clusters. The diffusion coefficients reaches values of about $D = 1.3 \cdot 10^{-6} \text{ m}^2/\text{s}$ at the highest dust temperatures of about $T = 4 \cdot 10^4 \text{ K}$. The values for the diffusion coefficient are decisively larger than in the 2D case [61, 81]. A reason for this is the higher dimensionality of the system that allows more paths to change configurations. ||

As discussed in Sec. 5, from the diffusion constant an approximate melting temperature can be extrapolated which is then found to be $T_M \approx 2010 \text{ K}$ for $N = 60$. Interestingly, this is smaller than the kinetic temperature of this cluster even in the absence of heating which is $T_{\text{kin}} = 2930 \text{ K}$ [86]. This relatively high kinetic temperature, even in the unheated case, is explained by additional heating processes by the wake-field instability caused by streaming ions in the plasma sheath [90–92].

7. Discussion and outlook

7.1. Discussion of the results

In this review, we discussed the various opportunities provided by laser beams as manipulation tools for dusty plasmas. We focused on the use of lasers as heating instruments for dust particles. As discussed in the introduction, various further uses, like the excitation of shear stress [16, 17] or of the rotation of a cluster shell [18], are possible as well, but this goes beyond the scope of this review. The availability of reliable heating tools is essential for the experimental investigation of phase transitions and instabilities in dust crystals. The enhanced manipulation setup for finite 2D dust

|| From the relation of the diffusion coefficient to the mean squared displacements, Eq. (4), one would expect a dimensionality-related increase by a factor $3/2$ which, however, is not sufficient to explain the observed difference of the experimental values. This problem is still under investigation.

clusters, presented in Sec. 3.1, has proven to be usable as a tunable thermostat in both experiment and LMD simulation. The experiments confirmed that the used laser heating scheme provides a homogeneous power input over the entire cluster and over all frequencies. As desirable for a true thermal heating, the isotropy and the Maxwellian shape of the velocity distribution are preserved to very high accuracy. Various laser scanning concepts have been studied in the simulations allowing to predict the optimal parameters for the experiments.

The laser heating method was used to perform temperature scans of small 2D dust clusters with different particle numbers. The instantaneous normal mode analysis allowed us to calculate the diffusion constant and, by this, to determine an approximate melting temperature. This melting temperature is found to be crucially dependent on the exact particle number, as a consequence of different cluster symmetries. At the same time the INM analysis does not allow to discriminate between intra-shell and inter-shell melting. As another more sensitive quantity we studied the center-two-particle distribution function which displays both intra-shell and inter-shell correlation.

The heating method for 3D dust clusters has to work with two opposing laser beams, due to the required space for diagnostics and illumination of the cluster. Hence, the heating quality with respect to the isotropy and the Maxwellian shape of the velocity distribution is not as perfect as for 2D clusters. Nevertheless, as in 2D, the quality of this heating technique is sufficient to manipulate the dust temperature (and hence the coupling strength) in a controlled manner, without affecting the plasma parameters. Due to the spherical symmetry of 3D Yukawa balls, structural parameters which take into account this symmetry are required in order to investigate the structure and the melting behavior of these systems. The most sensitive quantity turned out to be the center-two-particle distribution function which displays both intra-shell and inter-shell correlation and allows us to distinguish solid clusters with a highly ordered structure from molten clusters. While important aspects of the melting behavior in 3D are now understood, accurate data for the phase diagram and its the particle number dependence are still missing. The presented experimental tool—laser heating—, combined with the diagnostic based on the center-two-particle distribution function should allow to study these questions in detail in the near future.

7.2. Extension to transport properties of inhomogeneous strongly coupled systems

Both experiments and LMD simulations have shown that an appropriate heating scheme allows for a homogeneous heating of the entire 2D cluster [74, 75]. However, this heating method can also be used to heat only a selected spatial region. As long as the heated region is larger than the laser spot size, local heating is simply realized by restricting the area which is scanned by the laser spots. Kudelis *et al.* suggested an experiment where only the central region of a 2D Yukawa cluster is heated by four randomly moving laser spots and performed LMD simulations for this scenario [76]. The thermal conductivity associated with the radial temperature profile, see Fig. 14 (bottom), is found to be constant over a wide range in coupling strengths, including the phase transition between solid and liquid [76]. This result is in good agreement with experimental data for the heat transport in an extended 2D dust crystal by Nosenko *et al.* [23]. The upper part of Fig. 14 shows the spatial particle density of the Yukawa cluster that is heated in the inner region. While a pronounced shell structure is found at the cold outer region, the center of the cluster is molten.

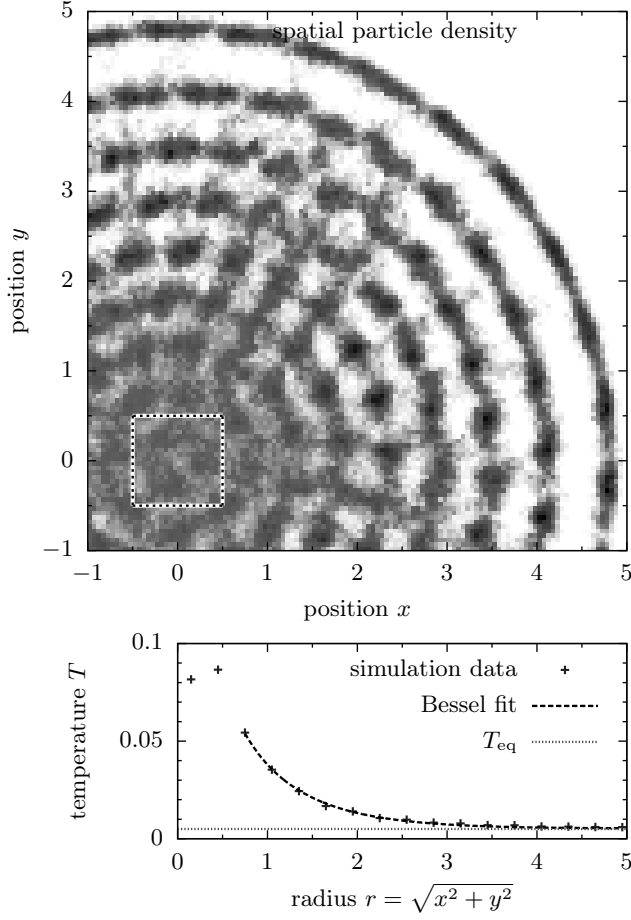


Figure 14. Top: Spatial density of a Yukawa cluster with $N = 200$ particles. Four randomly moving laser spots heat the inner square marked by the dashed rectangle. Bottom: Radial temperature profile and the fit by the analytical model presented in [76]. The temperature towards the border approaches the equilibrium temperature T_{eq} of the unheated cluster.

It remains an interesting task to verify these predictions in an experiment and, thus, employ laser heating for the measurement of heat transport in strongly correlated dusty plasmas. Another interesting task is to study the influence of an electric or magnetic field on the transport coefficients.

7.3. Control of time-dependent processes in complex plasmas

The applications discussed so far all considered stationary states. However, the laser heating method also allows for the study of time-dependent processes. The power input can be turned on and off practically instantaneously (relative to the slow time scale of the heavy dust particles) by switching on and off the laser power. A possible application is a temperature quench during which the system is abruptly cooled (or heated). This allows, for example, to study the time-dependent relaxation from a fluid

into a crystalline state. Hartmann *et al.* realized a quenching process experimentally by temporarily introducing a 20 Hz sinusoidal modulation to the dc self-bias of the powered lower electrode. This dc field causes a vertical shaking of the dust grains that allows to melt the crystal [93]. But, as discussed above, this bias modulation also affects the plasma parameters. Therefore, it would be highly desirable to realize such a quench by means of laser heating, as discussed in this review.

A particularly interesting application would be a temperature quench in the presence of a strong magnetic field. Ott *et al.* found in MD simulations that a magnetic field may prevent crystallization. This is unexpected since, due to the Bohr von Leeuwen theorem, a magnetic field should not affect the static properties of a classical system. The reason for the observed effect is that a strong magnetic field may prevent conversion of potential energy into kinetic energy creating a bottleneck for a phase transition. Above at critical magnetic field strength, the relaxation time τ_r for the crystallization increases exponentially [94]. It would be very interesting to verify these simulation results in a laser heating experiment. So far magnetizing dust particles in an experiment has not been possible which is due to the low specific charge Q_d/m of the dust grains. An alternative way to effectively “magnetize” the dust component is to put the cluster into rotation via a rotation of the neutral gas [95]. The Coriolis force then has the same functional form, $\vec{F}_C \propto \vec{v} \times \vec{\omega}$, as the Lorentz force and can be interpreted as a pseudo-magnetic field which is known as Larmor’s theorem. This idea has in fact been realized in dusty plasma experiments. It was shown that important properties such as collective modes of magnetized strongly correlated plasmas can be accurately reproduced [96–98]. In combination with the laser heating method, this technique will allow to quench finite dust clusters in experiments and to investigate the influence of the magnetization on the relaxation time for crystallization.

Acknowledgements. We acknowledge financial support by the Deutsche Forschungsgemeinschaft via SFB-TR 24, grants A3, A7 and A9 and a grant for CPU time at the HLRN (grant SHP006).

References

References

- [1] Ivlev A, Löwen H, Morfill G and Royall C P 2012 *Complex Plasmas and Colloidal Dispersions: Particle-Resolved Studies of Classical Liquids and Solids* Series in Soft Condensed Matter (World Scientific Pub Co)
- [2] Meichsner J, Bonitz M, Piel A and Feske H 2012 *Contrib. Plasma Phys.* **52** 789794
- [3] Bonitz M, Horing N and Ludwig P 2010 *Introduction to Complex Plasmas* 1st ed (Springer Berlin Heidelberg) ISBN 3642105912
- [4] Melzer A, Trottenberg T and Piel A 1994 *Phys. Lett. A* **191** 301–308
- [5] Bonitz M, Henning C and Block D 2010 *Rep. Prog. Phys.* **73** 066501
- [6] Ott T, Stanley M and Bonitz M 2011 *Phys. Plasmas* **18** 063701
- [7] Arp O, Block D, Piel A and Melzer A 2004 *Phys. Rev. Lett.* **93** 165004
- [8] Henning C, Baumgartner H, Piel A, Ludwig P, Golubnichiy V, Bonitz M and Block D 2006 *Phys. Rev. E* **74** 056403
- [9] Henning C, Ludwig P, Filinov A, Piel A and Bonitz M 2007 *Phys. Rev. E* **76** 036404

- [10] Ivanov Y and Melzer A 2005 *Phys. Plasmas* **12** 072110
- [11] Melzer A, Homann A and Piel A 1996 *Phys. Rev. E* **53** 2757–2766
- [12] Ashkin A 2000 *IEEE J. Sel. Top. Quantum Electron.* **6** 841–856
- [13] Bloch I 2005 *J. Phys. B: At. Mol. Opt. Phys.* **38** S629
- [14] Lu W, Tzoufras M, Joshi C, Tsung F S, Mori W B, Vieira J, Fonseca R A and Silva L O 2007 *Phys. Rev. Spec. Top. Accel Beams* **10** 061301
- [15] Roth M, Cowan T E, Key M H, Hatchett S P, Brown C, Fountain W, Johnson J, Pennington D M, Snavely R A, Wilks S C, Yasuike K, Ruhl H, Pegoraro F, Bulanov S V, Campbell E M, Perry M D and Powell H 2001 *Phys. Rev. Lett.* **86** 436–439
- [16] Nosenko V and Goree J 2004 *Phys. Rev. Lett.* **93** 155004
- [17] Feng Y, Goree J and Liu B 2012 *Phys. Rev. Lett.* **109** 185002
- [18] Klindworth M, Melzer A, Piel A and Schweigert V A 2000 *Phys. Rev. B* **61** 8404
- [19] Melzer A, Nunomura S, Samsonov D, Ma Z W and Goree J 2000 *Phys. Rev. E* **62** 4162–4176
- [20] Nosenko V, Goree J, Ma Z W and Piel A 2002 *Phys. Rev. Lett.* **88** 135001
- [21] Wolter M and Melzer A 2005 *Phys. Rev. E* **71** 036414
- [22] Nosenko V, Goree J and Piel A 2006 *Phys. Plasmas* **13** 032106
- [23] Nosenko V, Zhdanov S, Ivlev A V, Morfill G, Goree J and Piel A 2008 *Phys. Rev. Lett.* **100** 025003
- [24] Schella A, Miksch T, Melzer A, Schablinski J, Block D, Piel A, Thomsen H, Ludwig P and Bonitz M 2011 *Phys. Rev. E* **84** 056402
- [25] Bedanov V M and Peeters F 1994 *Phys. Rev. B* **49** 2667
- [26] Apolinario S W S and Peeters F M 2007 *Phys. Rev. E* **76** 031107
- [27] Kong M, Partoens B and Peeters F M 2003 *Phys. Rev. E* **67** 021608
- [28] Hasse R W and Avilov V V 1991 *Phys. Rev. A* **44** 4506–4515
- [29] Schiffer J P 1988 *Phys. Rev. Lett.* **61** 1843–1846
- [30] Ludwig P, Kosse S and Bonitz M 2005 *Phys. Rev. E* **71** 046403
- [31] Bonitz M, Block D, Arp O, Golubnychiy V, Baumgartner H, Ludwig P, Piel A and Filinov A 2006 *Phys. Rev. Lett.* **96** 075001
- [32] Baumgartner H, Asmus D, Golubnychiy V, Ludwig P, Kählert H and Bonitz M 2008 *New J. Phys* **10** 093019
- [33] Wrighton J, Dufty J W, Kählert H and Bonitz M 2009 *Phys. Rev. E* **80** 066405
- [34] Wrighton J, Dufty J, Bonitz M and Kählert H 2010 *Contrib. Plasma Phys.* **50** 2630
- [35] Bruhn H, Kählert H, Ott T, Bonitz M, Wrighton J and Dufty J W 2011 *Phys. Rev. E* **84** 046407
- [36] Wrighton J, Kählert H, Ott T, Ludwig P, Thomsen H, Dufty J and Bonitz M 2012 *Contrib. Plasma Phys.* **52** 4548
- [37] Käding S, Block D, Melzer A, Piel A, Kählert H, Ludwig P and Bonitz M 2008 *Phys. Plasmas* **15** 073710

- [38] Block D, Kroll M, Arp O, Piel A, Käding S, Ivanov Y, Melzer A, Henning C, Baumgartner H, Ludwig P and Bonitz M 2007 *Plasma Phys. Controlled Fusion* **49** B109
- [39] Kählert H, Ludwig P, Baumgartner H, Bonitz M, Block D, Käding S, Melzer A and Piel A 2008 *Phys. Rev. E* **78**(3) 036408
- [40] Baumgartner H, Block D and Bonitz M 2009 *Contrib. Plasma Phys.* **49** 281302
- [41] Golubnichiy V, Baumgartner H, Bonitz M, Filinov A and Fehske H 2006 *J. Phys. A: Math. Gen.* **39** 4527
- [42] Schiffer J P 2002 *Phys. Rev. Lett.* **88** 205003
- [43] Schweigert V A and Peeters F 1995 *Phys. Rev. B* **51** 7700
- [44] Filinov A V, Lozovik Y E and Bonitz M 2000 *phys. stat. sol. (b)* **221** 231
- [45] Filinov A V, Bonitz M and Lozovik Y E 2001 *Phys. Rev. Lett.* **86** 3851
- [46] Apolinario S, Partoens B and Peters F 2007 *New J. Phys.* **9** 283
- [47] Ludwig P, Thomsen H, Balzer K, Filinov A and Bonitz M 2010 *Plasma Phys. Controlled Fusion* **52** 124013
- [48] Daligault J 2006 *Phys. Rev. Lett.* **96** 065003
- [49] Ott T and Bonitz M 2011 *Phys. Rev. Lett.* **107**(13) 135003
- [50] Hou L J, Piel A and Shukla P K 2009 *Phys. Rev. Lett.* **102**(8) 085002
- [51] Ott T, Bonitz M and Hartmann P 2009 *Phys. Rev. Lett.* **103**(9) 099501
- [52] Ott T and Bonitz M 2009 *Contrib. Plasma Phys.* **49**(10) 760
- [53] Ott T and Bonitz M 2009 *Phys. Rev. Lett.* **103**(19) 195001
- [54] Ott T, Löwen H and Bonitz M 2014 *Phys. Rev. E* **89**(1) 013105
- [55] Vaulina O S, Adamovich X G, Petrov O F and Fortov V E 2008 *Phys. Rev. E* **77** 066404
- [56] Seeley G and Keyes T 1989 *J. Chem. Phys.* **91** 5581–5586
- [57] Stratt R M 1995 *Acc. Chem. Res.* **28** 201–207
- [58] Keyes T 1997 *J. Phys. Chem. A* **101** 2921–2930
- [59] Vijayadamodar G V and Nitzan A 1995 *J. Chem. Phys.* **103** 2169–2177
- [60] Keyes T, Vijayadamodar G V and Zurcher U 1997 *J. Chem. Phys.* **106** 4651–4657
- [61] Melzer A, Schella A, Schablinski J, Block D and Piel A 2013 *Phys. Rev. E* **87** 033107
- [62] Fisher R, Avinash K, Thomas E, Merlino R and Gupta V 2013 *Phys. Rev. E* **88** 031101
- [63] Piel A and Melzer A 2002 *Plasma Phys. Control. Fusion* **44** R1–R26
- [64] Homann A, Melzer A, Peters S, Madani R and Piel A 1997 *Phys. Rev. E* **56** 7138–7141
- [65] Annaratone B 1997 Crystal and fluid-like assemblies in plasma sheaths *International Conference on Phenomena in Ionized Gases* vol 07 C4 pp 155–165
- [66] Takahashi K, Oishi T, Shimomai K, Hayashi Y and Nishino S 1998 *Phys. Rev. E* **58** 7805–7811
- [67] Homann A, Melzer A, Peters S, Madani R and Piel A 1998 *Phys. Lett. A* **242** 173–180

- [68] Homann A, Melzer A and Piel A 1999 *Phys. Rev. E* **59** 3835–3838
- [69] Melzer A, Schweigert V A and Piel A 2000 *Physica Scripta* **61** 494–501
- [70] Samarian A A and Vladimirov S V 2009 *Contrib. Plasma Phys.* **49** 260–280
- [71] Kroll M, Schablinski J, Block D and Piel A 2010 *Phys. Plasmas* **17** 013702
- [72] Nosenko V, Goree J, Ma Z W, Dubin D H E and Piel A 2003 *Phys. Rev. E* **68** 056409
- [73] Piel A, Nosenko V and Goree J 2006 *Phys. Plasmas* **13** 042104
- [74] Schablinski J, Block D, Piel A, Melzer A, Thomsen H, Kählert H and Bonitz M 2012 *Phys. Plasmas* **19** 013705–013705–10
- [75] Thomsen H, Kählert H, Bonitz M, Schablinski J, Block D, Piel A and Melzer A 2012 *Phys. Plasmas* **19** 023701–023701–10
- [76] Kudelis G, Thomsen H and Bonitz M 2013 *Phys. Plasmas* **20** 073701–073701–7
- [77] Mannella R 2004 *Phys. Rev. E* **69** 041107
- [78] Spreiter Q and Walter M 1999 *J. Comput. Phys.* **152** 102–119
- [79] Chin S A 2008 *Phys. Rev. E* **77**(6) 066401
- [80] Ott T, Baiko D A, Kählert H and Bonitz M 2013 *Phys. Rev. E* **87** 043102
- [81] Melzer A, Schella A, Schablinski J, Block D and Piel A 2012 *Phys. Rev. Lett.* **108** 225001
- [82] Böning J, Filinov A, Ludwig P, Baumgartner H, Bonitz M and Lozovik Y E 2008 *Phys. Rev. Lett.* **100** 113401
- [83] Das S P 2004 *Rev. Mod. Phys.* **76** 785–851
- [84] Arp O, Block D, Klindworth M and Piel A 2005 *Phys. Plasmas* **12** 122102
- [85] Block D, Käding S, Melzer A, Piel A, Baumgartner H and Bonitz M 2008 *Phys. Plasmas* **15** 040701
- [86] Schella A, Mulsow M, Melzer A, Schablinski J and Block D 2013 *Phys. Rev. E* **87** 063102
- [87] Himpel M, Buttenschön B and Melzer A 2011 *Rev. Sci. Instrum.* **82** 053706
- [88] Schella A, Mulsow M, Melzer A, Kählert H, Block D, Ludwig P and Bonitz M 2013 *New J. Phys.* **15** 113021
- [89] Apolinario S, Partoens B and Peters F 2008 *Phys. Rev. B* **77** 035321
- [90] Schweigert V A, Schweigert I V, Melzer A, Homann A and Piel A 1996 *Phys. Rev. E* **54** 4155
- [91] Schweigert V A, Schweigert I V, Melzer A, Homann A and Piel A 1998 *Phys. Rev. Lett.* **80** 5345
- [92] Melandsø F 1997 *Phys. Rev. E* **55** 7495
- [93] Hartmann P, Douglass A, Reyes J C, Matthews L S, Hyde T W, Kovács A and Donk Z 2010 *Phys. Rev. Lett.* **105** 115004
- [94] Ott T, Löwen H and Bonitz M 2013 *Phys. Rev. Lett.* **111** 065001
- [95] Carstensen J, Greiner F and Piel A 2010 *Physics of Plasmas* **17** 083703
- [96] Kählert H, Carstensen J, Bonitz M, Löwen H, Greiner F and Piel A 2012 *Phys. Rev. Lett.* **109**(15) 155003

- [97] Bonitz M, Kählert H, Ott T and Löwen H 2013 *Plasma Sources Sci. Technol.* **22** 015007
- [98] Hartmann P, Donkó Z, Ott T, Kählert H and Bonitz M 2013 *Phys. Rev. Lett.* **111**(15) 155002